Wave-layered dendrite-free lithium deposition with unprecedented long-term cyclability.

FENG, J., GE, B., WANG, J., ZHANG, L., LIU, D., ZOU, G., TSE, J.S., FERNANDEZ, C., YAN, X. and PENG, Q.

2023

Wave-Layered Dendrite-Free Lithium Deposition with Unprecedented Long-Term Cyclability

Jiawen Feng[1], *Bingcheng Ge*[1,2*], *Jing Wang*[1], *Lu Zhang*[1], *Di Liu*[1], *Guodong Zou*[1], *John S. Tse*[3], *Carlos Fernandez*[4], *Xiaobing Yan*[5], *Qiuming Peng*[1*]

[1]State Key Laboratory of Metastable Materials Science and Technology, Yanshan University, Qinhuangdao, 066004, P.R. China

[2]Department of Mechanical Engineering, Research Institute for Smart Energy, The Hong Kong Polytechnic University, Hong Kong, China

[3]Department of Physics, University of Saskatchewan, Saskatoon, SK, S7N5B2, Canada

[4]School of Pharmacy and Life Sciences, Robert Gordon University, Aberdeen, AB107GJ, United Kingdom

[5]Key Laboratory of Brain-Like Neuromorphic Devices and Systems of Hebei Province, College of Electronic and Information Engineering, Hebei University, Baoding 071002, P.R. China

Corresponding author: pengqiuming@ysu.edu.cn

bingcheng.ge@polyu.edu.hk

Abstract

Lithium dendrite growth on the anode during cycling leads to poor stability and severe safety issue, hampering long-term cycle for high-energy batteries. Herein, we firstly found that dendrite-free Li can be deposited layer-by-layer on the surface of lithiophilic Li_3N (001) or (111) facet, and then synthesized a composite electrode of Li_3N involving a high fraction of (001) facet on porous carbon cloth (P-CC), wherein Li_3N *in-situ* formed by immersing of P-CC in a solution of molten Li, offering outstanding electrochemical and battery performance. Unique waved-layered dendrite free Li deposition has been detected during the Li-plating/stripping process. This P-CC/Li_3N/Li anode exhibits a cycle lifespan as long as 2000 h with low overpotential of ~20 mV at 1 mA cm^{-2} in a symmetrical cell, which overwhelms all similar systems reported so far. Attractively, long-term operations of 35, 200, and 400 h at 10 mA cm^{-2} can be achieved at temperatures of -10, 25, and 50 °C, respectively. Both experimental and density functional theory calculations confirm that the P-CC/Li_3N serves as an appropriate host for Li infusion through an efficient ion conductive network, inducing the nucleation and growth of metallic lithium.

Keywords: Li metal anode, Dendrite-free, Nucleation, Growth

1. Introduction

As the most promising candidate for next-generation batteries, Li metal batteries (such as Li-air and Li-S) have received considerable attention for their ultrahigh theoretical capacity (3860 mAh g^{-1}), the lowest electrochemical potential (-3.040 V versus standard hydrogen electrode), and low density (0.534 g cm^{-3}).[1-3] Unfortunately, Li dendrite issue in relative to uneven deposition not only reduces the utilization of active Li, resulting in a short cycling life,[4] but also causes safety risk, wherein the rooted dendrite growth enables the connection between electrodes, leading to short circuit or even an explosion.[5] To date, numerous efforts have been devoted to stabilizing the structure of Li metal anode to prevent the formation of Li-dendrites, it is still of great challenge towards long cycle life for high-energy batteries under industrial conditions.

Significant progress has been made to eliminate aforementioned problem, and available approaches include the application of artificial solid electrolyte interface phases (SEI), electrolyte additives, solid electrolytes, and nanostructured Li anodes.[6-8] These strategies mainly focus on the formed Li-plated morphology, whereas an initial Li nucleation/growth process hardly involves, which remarkably determines final Li morphology.[9, 10] For instance, the adsorption energy exceeding the cohesive energy of bulk Li enables a strong interaction between Li and the substrate, thus guiding a uniform Li nucleation and deposition.[11-14] In contrast, a weak interaction between Li atom and substrate corresponding to its low adsorption energy results in isolated cluster growth.[15] To reveal the effect of the substrate on Li deposition, Cui *etc.* [16] studied the nucleation of Li on various metal substrates. The results show that Li tended to deposit on Au rather than on Cu or the Au/Cu coexisted substrate,

since the adsorption energy of Li on Au is larger than that of Cu. In addition, based on the Volmer–Weber mode,[17] surface energy and migration energy of Li are two important thermodynamic factors for Li nucleation. In this regard, it is believed that the modification of the substrate surface is one of effective paths to alter Li nucleation process, preventing Li dendrite growth.

More recently, Li-containing compounds, such as Li_3N, Li_3Bi, LiAl *etc*. have been confirmed to effectively suppress Li dendrite growth. [18, 19] For example, Li_3N exhibits a high Li^+ conductivity close to 10^{-3} S cm^{-1} at room-temperature.[18, 19] Several research groups have attempted to form a layer of Li_3N between lithium and electrolyte as a protective layer, resulting in good cycablility.[5, 20, 21] Alternatively, nitride particles(such as Mg_3N_2) are dispersed in ether electrolyte to form a composite coating with metallic Li, which could induce a Li reaction and then generate a Li_3N enriched SEI layer.[22] However, those method still exists three main shortages: i) the mechanism of Li nucleation on Li_3N remains unclear, which severely limits the deep design of nucleate cores; ii) cracks are easily generated on electrode surface due to the poor mechanical properties of Li_3N, reducing battery performances; iii) long-term nitriding has been detrimental to the electrochemical performance of Li_3N modified Li electrode, and it becomes a technique bottleneck to prepare high quality electrode by appropriate nitriding process.[23]

To tackle these issues, we firstly clarified the nucleation and growth process of Li on the different facets of Li_3N by density functional theory (DFT) calculations. Subsequently, based on optimal facets, we synthesized a composite electrode of Li_3N containing the high ratio of (001) facets on P-CC, wherein Li_3N *in-situ* formed by immersing of P-CC in a solution of

molten Li, are prepared. Finally, a unique wave-layered dendrite-free Li deposition has been achieved on this composite electrode, resulting in unprecedented long-term cyclability.

2. Experimental

2.1 Preparation of P-CC electrodes

The carbon cloth (CC, W0S1009) was obtained from Cetech Co., Ltd., which was directly used without further treatment. In a typical process, the original carbon cloth was cut into pieces of 2.0 cm × 5 cm, then both ends of the carbon cloth were clamped with conductive clips. The Joule heating was conducted to prepared porous carbon cloth (P-CC) in air condition by using a DC power supply (Shanghai Ruiling Electric Appliance Co., LTD) at a current of 20 A for 10 s.

2.2 Preparation of P-CC/Li_3N/Li electrodes

A suitable amount of Li was melted at 350 °C in an Ar/N_2 (95:5)-filled glovebox (both H_2O and O_2 were less than 0.1 ppm). Whereafter, a piece of P-CC was placed on the surface of the molten Li. Due to the lithophilicity of porous CC, molten Li was quickly impregnated into the CC scaffold, and finally a P-CC/Li_3N/Li electrode was obtained. The samples were named P-CC/Li_3N/Li. P-CC/Li electrode was obtained by immersing molten lithium in a glove box containing pure Ar gas.

2.3 Battery assembly

The Li-O_2 battery assembly was performed based on a CR2032 coin type battery. It was successively assembled by stacking a lithium metal anode (14 mm in diameter), a piece of glass fiber separator (16 mm in diameter, Whatman) soaked with 80 μL of electrolyte (1 M LiTFSI dissolved in TEGDME solution). The cathodes were cut into disks. Several holes (4

mm in diameter) were drilled in the cathode shell so that the O_2 can easily and quickly access the cathode. Then, the assembled batteries were placed in a 250 mL glass vessel filled with high-purity O_2. The pure O_2 was pumped into the glass vessel through the straight two-way piston conducted alternatively by vacuuming and ventilating for three times. After incubating for 10 h, the discharge and charge cycles of the batteries were tested. All potentials were referenced against Li/Li^+. For symmetric cells testing, the ether-based electrolyte which consists of 1 M LiTFSI in DOL: DME=1:1 vol. % with 1 wt. % $LiNO_3$ was employed. The test temperature was controlled by a programmable furnace.

2.4 DFT calculation

DFT calculations were conducted using VASP,[24-26] based on projector augmented wave (PAW) method.[27] A slab of Li_3N containing 10 layers with a vacuum of 15Å along c axis are simulated. The PBE exchange-correlation functional within the generalized gradient approximation (GGA) was employed.[28] The cutoff energy of the kinetic energy was 500eV. The k-mash in the Brillouin zone was 3×3×1 via Monkhorst-Pack method.[29] The energy convergence tolerance was 1.0×10-5eV/atom, and the force certification was 0.01eV/Å. The van der Waals (vdW) interaction was involved via the semi-empirical DFT-D2 field method. [30, 31] The adsorption energy (ΔE_{ads}) was calculated as following:

$$\Delta E_{ads} = E^* - (E_{slab} + \mu Li) \quad (1)$$

where E^* and E_{slab} were the total energy of the Li3N slab with/without adsorbed Li, μLi was the chemical potential defined as the total energy per Li atom in the bulk.

According to the XRD spectrum, four planes, including (001), (002), (110) and (111), were considered. One Li adsorption model was built to examine the adsorption ability of each

plane. Moreover, to simulate the growing trend, 9 Li atoms and 16 Li atoms with in-plane and out-of-plane arrangements in the initial structures were optimized, which indicates they were prone to spread in-plane. The energy difference (eV/Li), which was calculated as following:[32]

$$\Delta E = (E_N - E_{N-1} - n\mu_{Li}) /n \quad (2)$$

where E_N and E_{N-1} were the total energy of the slab with N and N-l layer Li, n was the number of Li atom per layer, and it was used to assess the growing thickness of Li layers.

3. Results and discussion

3.1 Facet characteristics of Li_3N

Systematic DFT calculations have been performed to reveal facet characteristics of Li_3N with Li. Theoretically, the dendrite growth can be effectively inhibited, providing that the in-plane growing on lithophilic substrate is preferred (**Figure 1**a).[10, 33] For starters, the adsorption energy of a single Li atom on various facets of Li_3N has been calculated, *i.e.*, (001), (002), (110) and (111) facets, in comparison with on (001) and (110) facets of Li substrate (Figure 1b-c). It is shown that the (001) and (111) facets of Li_3N exhibit stronger Li binding ability with lower adsorption energies, which indicates that these two facets are preferential for Li, in relative to those of pure Li substrate (Figure S1-3). The strong interaction between Li singlet and Li_3N (001) and Li_3N (111) surface can also be witnessed with the sharp charge density difference which suggests tight bonding between the adsorbate and the substrate (Figure 1d). As a consequence, it is preferential to nucleate on Li_3N instead of Li during the deposition process of Li.

In addition, the dendrite growth can also be inhibited, given that the in-plane growing on

lithophilic substrate is prior to out-of-plane growth. Therefore, the adsorption energies of multiple Li atoms in the above two growing manners have been further simulated, where we arranged 4, 9, and 16 Li atoms (dark green) on the Li_3N (001) facet in various stackings as examples (Figure 1e-h, and S2-S4). As a representative, for the case of 9 atoms, the energy of in-plane growth lowers by 0.048 eV/Li in contrast to an out-of-plane manner, which indicates that the titled growth is preferred than that of stacked growth, proving that the growth of dendrites would be effectively prohibited during deposition process. Consistent conclusion can be made for models containing 4, 16 Li atoms guaranteeing that the Li deposition process takes place layer-by-layer (Figure S3, S4).

Finally, as Li deposition is underway, the layer-by-layer growth manner will stop until the energy difference between layers (ΔE) approaches zero, and then dendrites start. Therefore, the slower the ΔE changes, the better for inhibiting the dendrites growth. Thus, the maximum layer of Li on the surface of Li_3N was evaluated by checking the variation of ΔE (Figure 1g, h and S5). Figure 1g shows that it demands 16 layers of Li atoms for Li_3N (001), to achieve $\Delta E = 0$ (Figure 1h). In turn, the adsorption energy of Li atoms on the Li metal surface becomes identical only last 2 layers Li growth (Figure S6). Besides, we understand the metal-metal interaction of Li on the Li_3N and Li via electron localization function (ELF, Figure S7-S8), where the in-plane growth on Li_3N gives rise to metallic bond which is more conducive to uniform deposition of lithium dendrites.[34]

3.2 Electrode characteristics

Inspired by the above predicted results of the existence of potential dendrite-free facets of Li_3N, a strategy to anchor Li_3N particles on porous carbon cloth (P-CC/Li_3N) has been

designed, wherein a high fraction of optimal facets is desirable for Li deposition and the disperse sites greatly reduce internal stress. Specifically, the pristine CC has been pretreated by a pulsed current of 20A for 10 s, thus, a typical coarse CC substrate has been attained. As evidenced by scanning electron microscopy (SEM) images (Figure S9), both the surface and cross section of the substrate have a porous structure. Moreover, the nitrogen adsorption test (BET method) and pore size distribution indicate that the P-CC contains a hierarchical pore with diameters from about 1.4~1.8 to 8.2~10.2 nm, which is of great benefit for lithiophilicity (Figure S10).[35] Raman spectrum (Figure S11a) reveals that defect density is increased after heat treatment in relative to the variation of I_D/I_G value from 0.95 to 1.09, [36] and shows that the intensity of D band at $\approx$1342 cm^{-1} is attributes to a disorder structure, and G band at $\approx$ 1587 cm-1 relates to highly a symmetrical sp^2 carbon structure.[37] This result has also been supported by the peak of defect carbon in terms of X-ray photoelectron spectroscopy (XPS, Figure S11b-c).[38]

Subsequently, the P-CC was immersed in molten Li in Ar or Ar/N_2 mixed conditions, in which violent adsorption of Li occurred spontaneously (Figure S12). As the treated carbon fiber is lithiophilic, the molten Li preferentially spreads along the carbon fiber and reacts with N_2 in a mixed atmosphere to form a hexagonal Li_3N structure on the surface of the carbon fiber. Driven by flow Li, particles preferentially distribute along the carbon fiber. As a result, some hexagonal-shaped Li_3N phases on the carbon fiber have been detected after removing Li layer, as shown by X-ray diffraction (XRD) and SEM (**Figure 2**a, b, Figure S13). The corresponding energy dispersive spectroscopy (EDS) mapping reveals the distribution of N and C elements in the electrode provides complementary evidence for the formation of Li_3N

(Figure 2c-e). The Rietveld analysis of the XRD data show that the mass ratio is about 0.7421/0.2579(Li/Li_3N) in the prepared P-CC/Li_3N/Li anode (Figure S14). Transmission electron microscopy (TEM) presents that Li_3N has a polycrystalline structure (Figure S15a), and high-resolution transmission electron microscopy (HRTEM) and Fast Fourier transform(FFT) of the whole HRTEM image showing superlattice reflections (002) and (101) (Figure 2f). The grain size of Li_3N in TEM is about 18.25 nm and the area fraction of Li_3N particles in SEM image is about 21.2%, respectively (Figure S15b-c). Additionally, the formation of Li_3N (~398 eV) has also been confirmed with the presence of the N *1s* peak (~55.2eV) in the XPS profiles of P-CC/Li_3N/Li (Figure 2g).[20, 21, 39, 40]

3.3 Electrochemical performances

To probe the Li-plating behaviors on the different anodes, the *in-situ* optical microscope and *ex-situ* surface morphology characterizations have been performed **(Figure 3** and S15-S16, Videos S1-S2). As shown in Figure 3a, Li dendrites appear immediately on the smooth surface of the reference Li electrode, resulting in the formation of numerous moss-like dendrites. In comparison, the uniform and flat Li layer is observed on the surface of the P-CC/Li_3N/Li electrode (Figure 3b). Moreover, no obvious dendrite structure has been detected with further retarding the deposition time, suggesting the formation of Li dendrites has been greatly suppressed.

The lithium-plating behaviors were further investigated by assembling electrodes in coin batteries. During the stripping process, Li metals in the anode are dissolved, and partial surfaces are exposed. Notably, uneven stripping pits are presented on the pure Li foil anode (Figure 3d-e). After stripping for 10 mAh cm^{-2}, a rough surface is observed for the pure Li

foil (Figure 3e). The cross-sectional images show that the pure Li surface fluctuates after stripping and dendrites after plating (Figure S16d-f). Comparatively, an intact porous CC with Li_3N skeleton is observed for the P-CC/Li_3N/Li anode after cycle treatment (Figure 3i). During the plating process, the Li metals are deposited on the anodes. Some spherical dendrites are observed on the surfaces of both the pure Li and P-CC/Li anode (Figure 3f, Figure S17). Conversely, Li is prone to deposit and grow on the Li_3N surface on the P-CC/Li_3N electrode (Figure 3j). More importantly, as the deposited Li amount increases to 10 mAh cm^{-2}, some bar-shaped or conglobate dendrites form on the surfaces of the pure Li anode (Figure 3g) and P-CC/Li anode (Figure S17), respectively. In contrast, the Li metal has been completely filled the space between the P-CC/Li_3N skeletons, showing a wave-layered dendrite-free lithium deposition (Figure 3k, Figure S16a-c).

To evaluate the structure integrity of the electrodes, the electrode morphology changes after cycles were explored (Figure S18). In the case of pure Li, the electrode surface is gradually covered by dendrites (10 cycles), and the electrode surface after 100 cycles is fully covered with Li dendrites (Figure S18a-b). On the contrary, flat surfaces of the P-CC/Li_3N/Li electrode are detected after 10 and 100 cycles (Figure S18c-d). The electrochemical impedance spectroscopy (EIS) of the symmetric cell at different cycles (Table S1) reveal that the interfacial impedance firstly decreases and then increases. It can be elucidated that the battery first undergoes activation in relation to the reduction of interfacial impedance. Comparatively, as Li dendrites grow at the interface, creating "dead Li" and by-products, the interface impedance increases (Figure S19a-b). For the electrodes containing Li_3N, the interfacial impedance hardly changes during cycling process (Figure S19c-d), indicating that

their good structure integrity.

3.4 Battery performance

Battery performance of the P-CC/Li_3N/Li anode has been evaluated in symmetric cell configuration using an ether-based electrolyte (1 M LiTFSI in DOL: DME=1:1 vol. % with 1 wt.% $LiNO_3$), at a current density of 1 mA cm^{-2} and a limited capacity of 1 mAh cm^{-2} (**Figure 4**a**)**, with the Li and P-CC/Li electrodes serving as the references. Notably, the potential of the pure Li electrode rose rapidly after 240 h cycles before the cell failed. The voltage hysteresis of the P-CC/Li anode increased largely after 400 hours. As a comparison, the P-CC/Li_3N/Li cell maintains stable voltage profiles with a small voltage of about 20 mV without obvious oscillation over 2000 h. Furthermore, even the current density increases from 5 to 10 mA cm^{-2}, the P-CC/Li_3N/Li anode still exhibits a long-term cyclability with low overpotentials (Figure 4b and S20a-b). The rate performances of three electrodes at different current densities from 0.5 to 5 mA cm^{-2} under a capacity of 1.0 mAh cm^{-2} (Figure S20c) shows that the P-CC/Li_3N/Li anode always exhibits substantially lower voltage hysteresis because Li_3N reduces the transfer resistance of Li^+ at the Li/electrolyte interface,[41] in which when the current density returns to 1 mA cm^{-2}, the voltage polarization is equivalent to the initial value. Moreover, even under the condition of higher area capacity of 10 mAh cm^{-2}, the outstanding electrochemical performance still remains (Figure S20d).

In addition, the P-CC/Li_3N/Li anode enables the stable operation at a wide temperature range (25, 50, 25, -10, and 25 °C, in sequence) and maintains the smallest potential change compared with Li and the P-CC/Li anodes (Figure 4c). Impressively, the galvanostatic cycling shows that the P-CC/Li_3N/Li anode can cycle 36 and 400 h at -10 and 50°C, which is

35 and 30 times longer than that of pure Li, respectively (Figure S21). To the best our knowledge, the excellent electrochemical performance of the P-CC/Li_3N/Li electrode is far higher than the previously reported carbon fiber or Li_3N modified anode (Figure 4d).[21, 23, 35, 42, 43] Notably, after the Li is completely stripped from the hybrid framework to 1 V *vs* Li^+/Li, the voltage curve (Figure S22) shows the total specific capacity of 1902 and 1635 mAh g^{-1}, respectively. No obvious plateaus are observed in three curves, indicating that only the infiltrated excess Li contributes to high capacity.[44]

We further applied the P-CC/Li_3N/Li anode to Li-O_2 full batteries with a P-CC cathode and the above ether-based electrolyte, wherein the pure Li anode and original CC cathode are involved. As shown in Figure 4e, the Li-O_2 battery assembled with a P-CC/Li_3N/Li as the anode and a P-CC as the cathode achieves a maximum discharge capacity of nearly 6.8 mAh cm^{-2} with a charging efficiency of nearly 98%, which are only 3.4 mAh cm^{-2} and 20% for the CC cathode. As evidenced by the SEM images, XRD and XPS patterns (Figure S23-S24), the morphologies of the discharge products on the two cathodes are completely different at same discharge capacity of 0.5 mA cm^{-2}. The nano-platelet discharge product deposited on the P-CC is beneficial to maintain the highly porous structure. When charging is completed, the discharge products on the P-CC are completely decomposed, but some discharge products remain on the CC, revealing higher charging efficiency for the former. Figure 4f exhibits the first discharge-charge voltage curves of the Li-O_2 battery based on different cathodes and anodes under a current density of 0.1 mA cm^{-2} with a capacity of 0.5 mAh cm^{-2}. The discharge/charge voltage platform for the P-CC cathode has been remarkably improved. The discharge voltage of the Li-O_2 battery with the P-CC cathode ends >2.0 V for 180 cycles.

Instead, after 25 cycles (Figure S25), the discharge voltage of the CC cathode falls below 2.0 V. This high cyclability has also been confirmed by the intact surface morphology even after 50 cycles (Figure S26). Furthermore, the rate capacity (Figure 4g) reveals that a higher discharge voltage plateau of the P-CC cathode can be observed compared with the CC cathode within a current density range from 0.1 to 1.0 mA cm^{-2}. The superior kinetics properties of the P-CC cathode are partially associated with the high porous and large specific surface area of the cathode, providing plentiful three-phase interface for fast and efficient mass transfer.[4]

4 Conclusion

In summary, combined with both theoretical models and experimental investigation, we prepared a new composite with special planes of Li_3N on the substrate of porous carbon cloth, achieving high electrochemical and battery performance in terms of wave-layered dendrite-free Li deposition. The robust, lithophilic interphase Li_3N with planes of (001) and (111) facilitate a homogenous Li nucleation at an initial plating stage and navigates the subsequent lateral Li plating. The lithium metal symmetric cell assembled with P-CC/Li_3N/Li as the anode exhibits unprecedented cycle lifespan of 2000 h with a low overpotential. Also, long-term operations of 35, 200, and 400 h at 10 mA cm^{-2} can be achieved in symmetrical cells within a wide temperature range from -10 to 50 °C. Based on the stable P-CC/Li_3N/Li anode and the P-CC cathode, the corresponding Li-O_2 battery presents a long-term structural stability. This lithiophilic interphase with optimal facets opens up a new and large-scale avenue to fully implement high capacity Li anode.

Supporting Information

Supporting Information is available from the Online Library or from the author.

Acknowledgements

We greatly acknowledge the financial support from National Natural Science Foundation-Outstanding Youth Foundation (grant No. 51971194，52171126), the Natural Science Foundation of Hebei Province for Innovation Groups Program (grant No. C2022203003), the Natural Science Foundation for Excellent Young Scholars of Hebei Province (grant No. E2022203167), and Ministry of Education Yangtze River Scholar Professor Program (grant No. T2020124) and the Foreign Intelligence Introduction Program of Hebei Province (grant No. 213000302)**.** CF would like to express his gratitude to PALS for support.

References

[1] C. Shu, J. Wang, J. Long, H. Liu, S. Dou, Adv. Mater., 31(2019) 1804587.

[2] Y. Liu, Y. Zhu, Y. Cui, Nat. Energy, 4(2019) 540-550.

[3] C. Xia, C.Y. Kwok, L.F. Nazar, Science, 361(2018) 777-781.

[4] B. Wu, Y. Yang, D. Liu, C. Niu, M. Gross, L. Seymour, H. Lee, P.M.L. Le, T.D. Vo, Z.D. Deng, E.J. Dufek, M.S. Whittingham, J. Liu, J. Xiao, J. Electrochem. Soc., 166(2019) A4141.

[5] H. Xu, Y. Li, A. Zhou, W. Nan, J.B. Goodenough, Nano Lett., 18 (2018) 7414-7418.

[6] T. Yang, P. Jia, Q. Liu, L. Zhang, C. Du, J. Chen, H. Ye, X. Li, Y. Li, T. Shen, Y. Tang, J. Huang, Angew. Chem. Int. Ed., 130 (2018) 12932-12935.

[7] X. Chi, M. Li, J. Di, P. Bai, L. Song, X. Wang, F. Li, S. Liang, J. Xu, J. Yu, Nature, 592 (2021) 551-557.

[8] M.G. Jeong, W.J. Kwak, J.Y. Kim, J.K. Lee, Y.K. Sun, H.G. Jung, Chem. Eng. J., 427

(2022) 130914.

[9] D. Yang, C. Zhao, R. Lian, L. Yang, Y. Wang, Y. Gao, X. Xiao, Y. Gogotsi, X. Wang, G. Chen, Y. Wei, Adv. Funct. Mater., 31 (2021) 2010987.

[10] J. Luan, Q. Zhang, H. Yuan, D. Sun, Z. Peng, Y. Tang, X. Ji, H. Wang, Adv. Sci., 6 (2019) 1901433.

[11] L. Chen, X. Chen, C. Duan, Y. Huang, Q. Zhang, B. Xiao, Phys. Chem. Chem. Phys., 20 (2018) 30304-30311.

[12] B. Xu, L. Wang, H.J. Chen, J. Zhao, G. Liu, M.S. Wu, Comput. Mater. Sci., 93 (2014) 86-90.

[13] R. Zhang, X.R. Chen, X. Chen, X.B. Cheng, X.Q. Zhang, C. Yan, Q. Zhang, Angew. Chem. Int. Ed., 129 (2017) 7872-7876.

[14] J.G. Hou, W. Xu, Y. Li, L. Yang, Y. Wang, J. Phys. Cond. Matt., 10 (1998) 9609.

[15] M.S. Kim, Deepika, S.H. Lee, M.S. Kim, W.I. Cho, Sci. Adv., 5 (2019) eaax5587.

[16] K. Yan, Z. Lu, H.W. Lee, F. Xiong, P.C. Hsu, Y. Li, J. Zhao, S. Chu, Y. Cui, Nat. Energy, 1 (2016) 1-8.

[17] X.B. Cheng, R. Zhang, C.Z. Zhao, Q. Zhang, Chem. Rev., 117 (2017) 10403-10473.

[18] T. Lapp, S. Skaarup, A. Hooper, Solid State Ionics, 11 (1983) 97-103.

[19] W. Li, G. Wu, C.M. Araújo, R.H. Scheicher, A. Blomqvist, R. Ahuja, Z. Xiong, Y. Feng, P. Chen, Energy Environ. Sci., 3 (2010) 1524-1530.

[20] Y. Liu, H. Su, M. Li, J. Xiang, X. Wu, Y. Zhong, X. Wang, X. Xia, C. Gu, J. Tu, J. Mater. Chem. A, 9 (2021) 13531-13539.

[21] J. Zhu, J. Chen, Y. Luo, S. Sun, L. Qin, H. Xu, P. Zhang, W. Zhang, W. Tian, Z. Sun,

Energy Storage Mater. 23 (2019) 539-546.

[22] Q.Y. Dong, B. Hong, H.L. Fan, H. Jiang, K. Zhang, Y.Q. Lai. ACS Appl. Mater. Interfaces, 12(2019) 627-636.

[23] Y.J. Zhang, W. Wang, H. Tang, W.Q. Bai, X. Ge, X.L. Wang, C.D. Gu, J.P. Tu, J. Power Sources, 277 (2015) 304-311.

[24]W. Kohn, Phys. Rev. Lett., 76(1996) 3168-3171.

[25]G. Kresse and J. Furthmüller. Comp. Mater. Sci., 1996, 6(1) 15-50.

[26]G. Kresse and J. Furthmüller. Phys. Rev. B, 54(1996) 11169-11186.

[27]J. P. Perdew, K. Burke and M. Phys. Rev. Lett., 77(1996): 3865-3868.

[28]M. S. Bahramy, M. H. F. Sluiter and Y. Kawazoe. Phys. Rev. B, 76(2007) 035124.

[29]H. J. Monkhorst and J. D. Pack. Phys. Rev. B, 13(1976) 5188-5192.

[30]S. Grimme. J. Comp. Chem., 27(2006) 1787-1799.

[31]S. Grimme, J. Antony, S. Ehrlich, et al. The J. Chem. Phys., 132(2010) 154104.

[32]J. K. Nørskov, J. Rossmeisl, A. Logadottir, et al. The J. Phys. Chem. B, 108(2004) 17886-17892.

[33] Z. Jingxu, Z. Qing, T. Tian, Y. Jiefu, C.D. Quilty, G.D. Renderos, L. Xiaotun, D. Yue, W. Lei, D.C. Bock, Science, 366 (2019) 645-648.

[34] D. Xie, Y.P. Zheng, M. Zahid, Y.F. Li, W.Y. Diao, F.Y. Tao, Z.F. Yang, H.Z. Sun, X.L. Wu, J.P. Zhang, J. Colloid Interface Sci., 609 (2022) 606-616.

[35] Y. Luo, T. Li, H. Zhang, W. Liu, X. Zhang, J. Yan, H. Zhang, X. Li, Angew. Chem. Int. Ed., 60 (2021) 11718-11724.

[36] G. Huang, J.H. Han, F. Zhang, Z.Q. Wang, H. Kashani, Adv. Mater., 31 (2019) 1805334.

[37] J. Wan, Y.X. Song, W.P. Chen, H.J. Guo, Y. Shi, Y.J. Guo, J.L. Shi, Y.G. Guo, F.F. Jia, F.Y. Wang, R. Wen, L.J. Wan, J. Am. Chem. Soc., 143 (2020) 839-848.

[38] H. Estrade-Szwarckopf, Carbon, 42 (2004) 1713-1721.

[39] Y. Zhou, Y. Han, H. Zhang, D. Sui, Z. Sun, P. Xiao, X. Wang, Y. Ma, Y. Chen, Energy Storage Mater., 14 (2018) 222-229..

[40] K. Park, J.B. Goodenough, Adv. Energy Mater., 7 (2017) 1700732.

[41] S. Jin, Y. Ye, Y. Niu, Y. Xu, H. Jin, J. Wang, Z. Sun, A. Cao, X. Wu, Y. Luo, H. Ji, L.J. Wan, J. Am. Chem. Soc., 142 (2020) 8818-8826.

[42] A. Ghosh, P. Cherepanov, C. Nguyen Ky, A. Ghosh, A. Kumar, A. Ahuja, M. Kar, D. MacFarlane, S. Mitra, Appl. Mater. Today, 23 (2021) 101062.

[43] S. Xia, X. Zhang, L. Luo, Y. Pang, J. Yang, Y. Huang, S. Zheng, Small, 17 (2021): 2006002.

[44] J. Wang, M. Yang, G. Zou, D. Liu, Q. Peng, Adv. Funct. Mater., 31 (2021) 2101180.

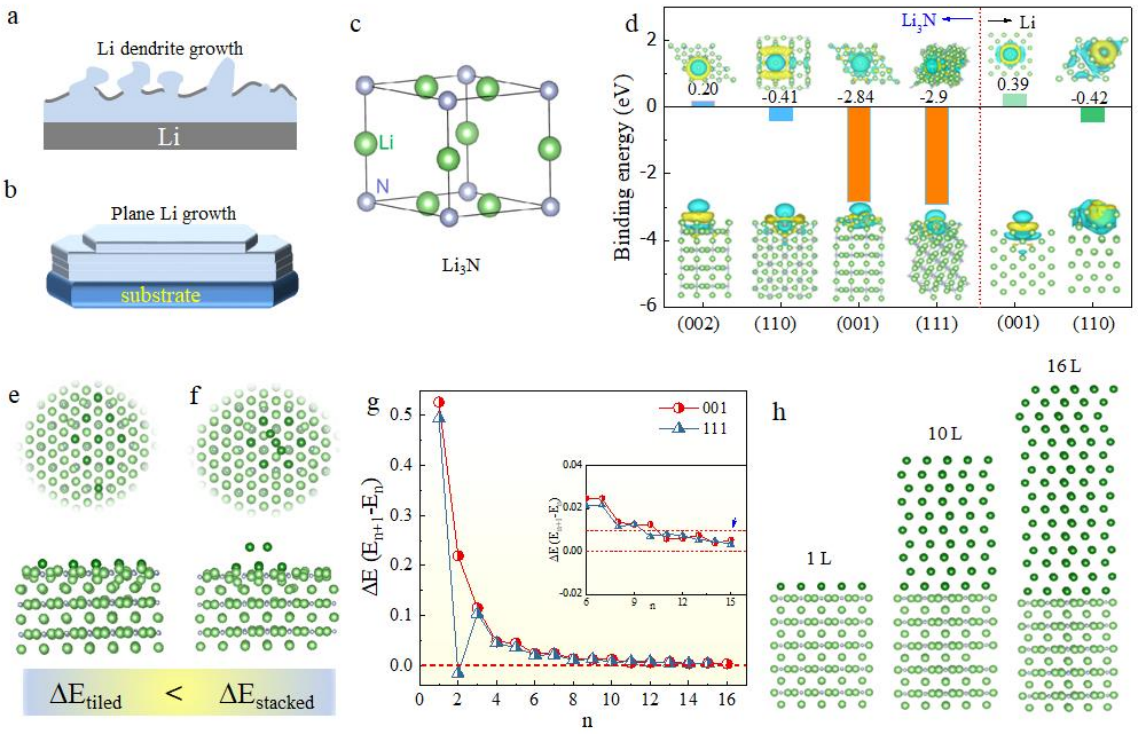

Figure 1. a-b) Scheme illustration of electrodeposition principle on lithophilic substrate. c) Schematic diagram of the crystal structure of Li_3N. d) Adsorption of Li atom on different facets of Li_3N, Li and differential charge density. Arrangement of 9 Li atoms on the Li_3N (001) facet: e) in plane, f) stacking arrangement. g) Energy difference of two adjacent layers (inset: 5-16 layers). h) Layout of multi-layer Li on the Li_3N (001) facet.

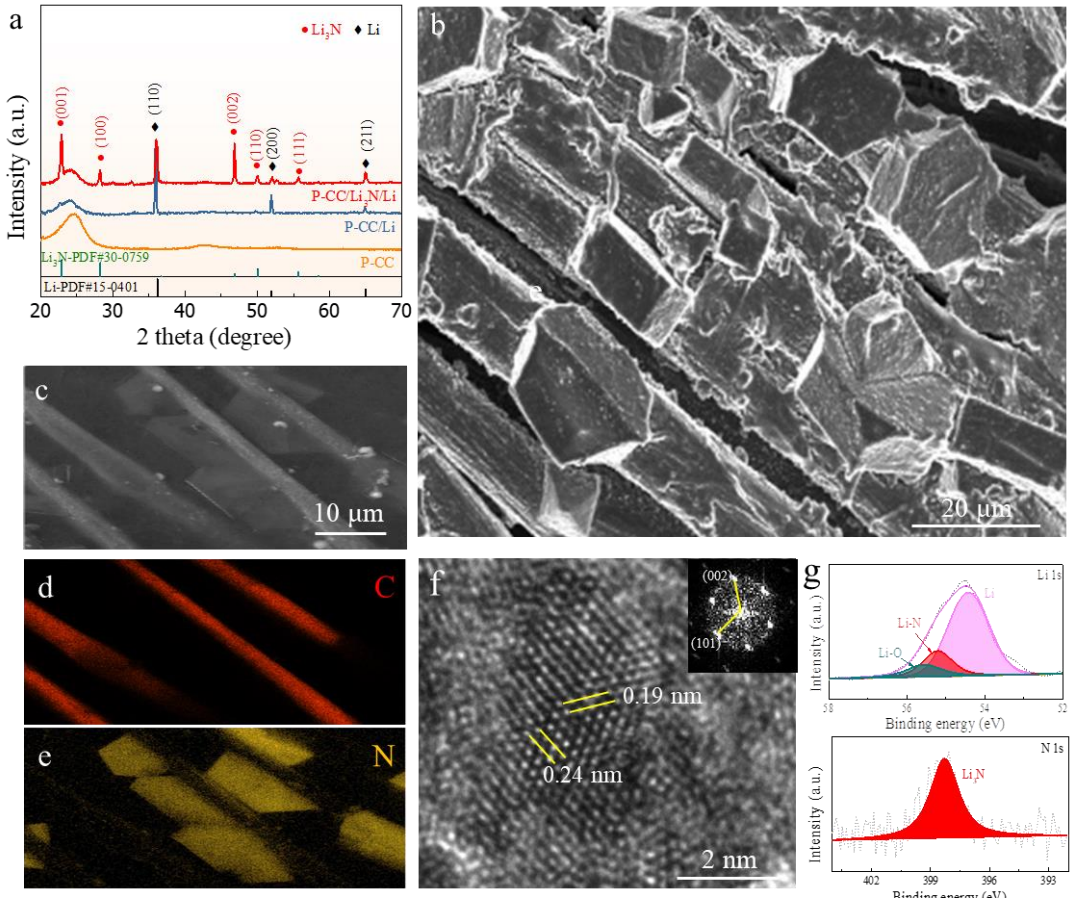

Figure 2. a) XRD characterization of the P-CC, P-CC/Li, P-CC/Li_3N/Li. b) SEM image of the P-CC/Li_3N, c-e) EDS mapping of the P-CC/Li_3N/Li. f) HRTEM and FFT images of the Li_3N, g) XPS high-resolution spectra of the P-CC/Li_3N electrode: N 1*s* and Li 1*s*.

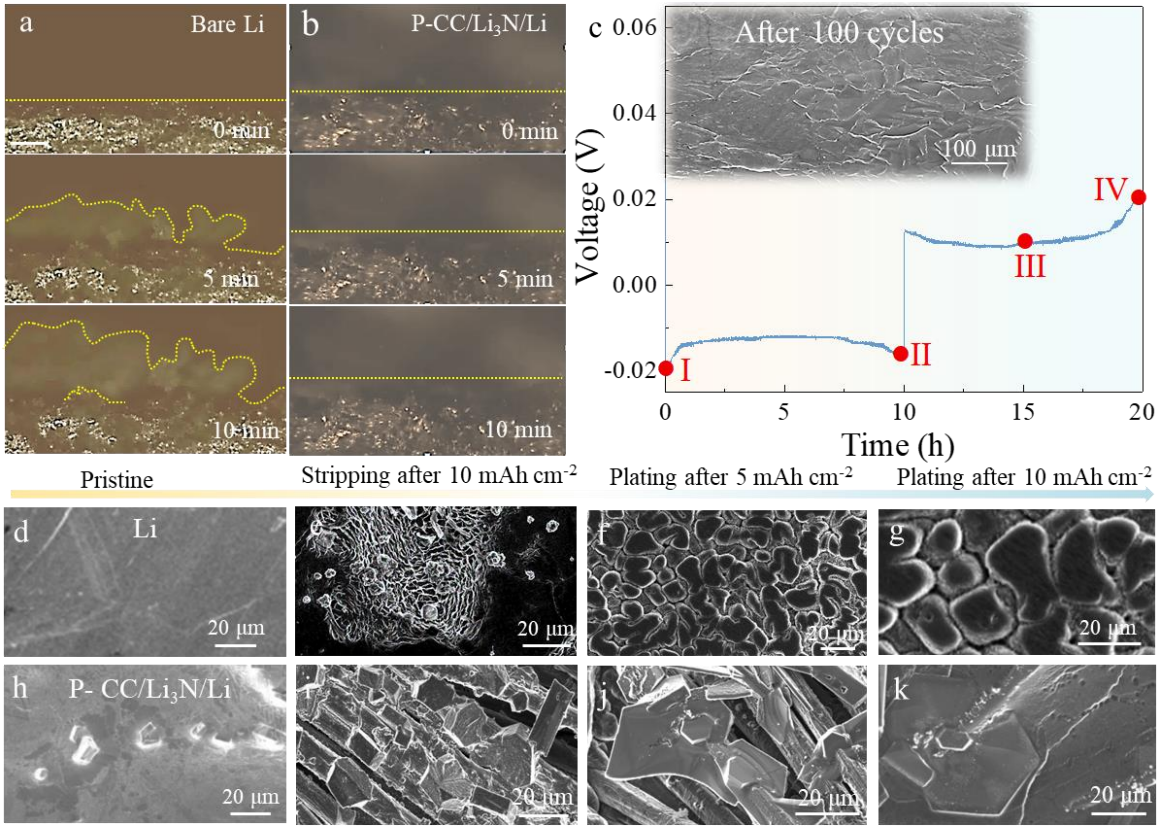

Figure 3. *In situ* optical microscope images of a) the Li metal anode and b) the P-CC/Li_3N/Li anode. c) Stripping/plating curves of battery using the P-CC/Li_3N/Li anode at 1 mA cm^{-2} with a capacity of 10 mAh cm^{-2}. Surface SEM images of the Li metal anode with a Li stripping of 5 mAh cm^{-2}(d) and 10 mAh cm^{-2}(e), and then plating of 5 mAh cm^{-2}(f) and 10 mAh cm^{-2}(g). Surface SEM images of the P-CC/Li_3N/Li anode with a Li stripping of 5 mAh cm^{-2}(h) and 10 mAh cm^{-2}(i), and then plating of 5 mAh cm^{-2}(j) and10 mAh cm^{-2} (k).

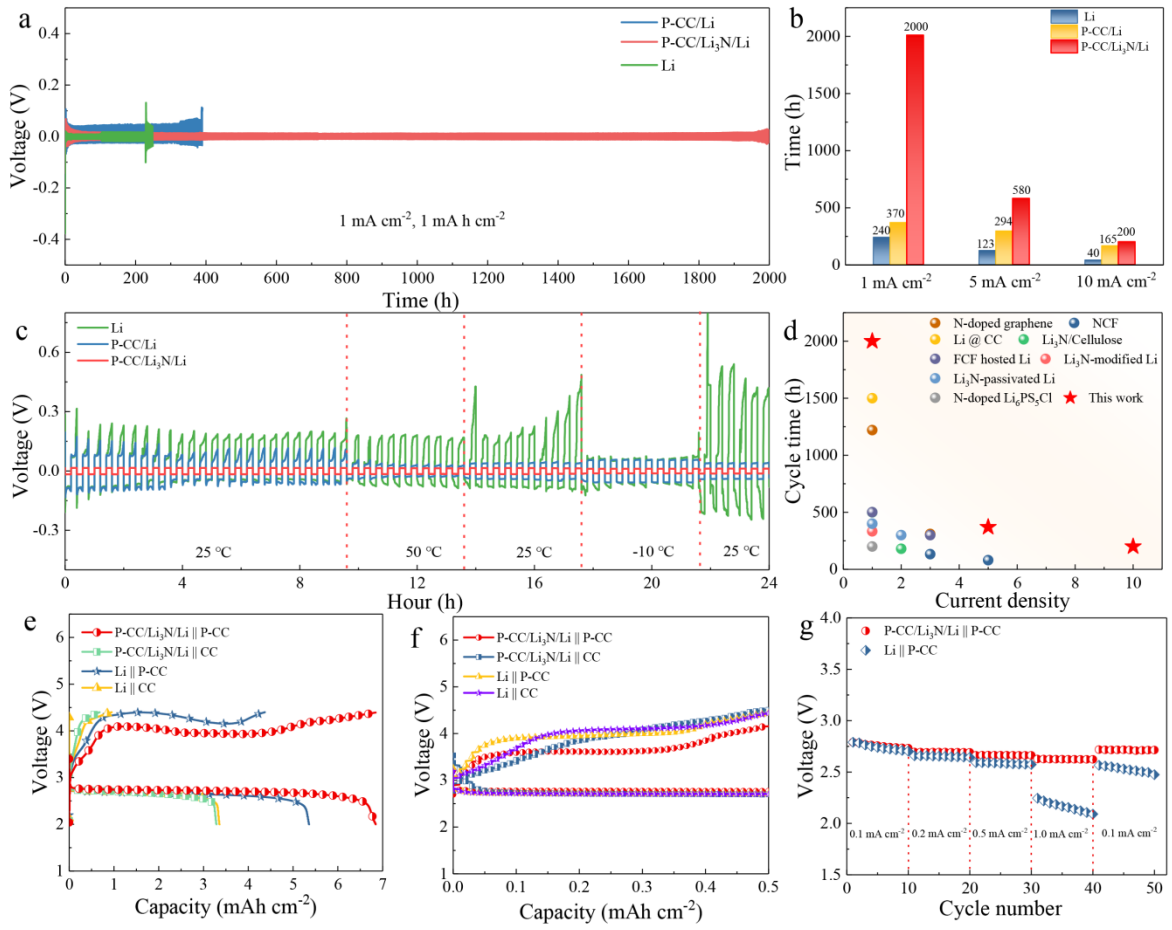

Figure 4. a) Galvanostatic cycling of the pure Li, P-CC/Li and P-CC/Li_3N/Li symmetric cells with a stripping/plating capacity of 1 mAh cm^{-2} at a current density of 1 mA cm^{-2}. (b) Comparison of electrochemical properties of symmetrical cells at different current densities. (c) Cycling stability of symmetric cells that incorporated the different electrodes, the temperature was switched repeatedly every 20 cycles between -10 °C and 50 °C. (d) Comparison of the current density and cycle lifespan of the P-CC/Li_3N/Li anode with those of various Li metal anodes. (e) Initial complete discharge curves of different electrodes at a current density of 0.1 mA cm^{-2}. (f) Initial charge-discharge cycles of different electrodes at a current density of 0.1 mA cm^{-2}. (g) The terminal cut-off voltage of different electrodes at different current densities.